IR Telescope and Sensor Characterization for Hypervelocity Asteroid Intercept Guidance

Joshua Lyzhoft* and Bong Wie†
Iowa State University, Ames, IA 50011, USA

This paper presents the performance characterization of an infrared sensor and selected optics for an asteroid intercept vehicle traveling at hypervelocity speeds. The feasibility of using an IR sensor for hypervelocity intercept of ballistic missiles has been demonstrated by Raytheon's Exoatmospheric Kill Vehicle (EKV). In our previous work, hypervelocity impact guidance using an infrared sensor was studied for an asteroid intercept mission. However, optical telescope design for the mission was not considered. In this paper, further investigation in how telescope design will effect the performance and precision impact location of the Hypervelocity Asteroid Intercept Vehicle is described.

Nomenclature

F	Overall System Focal Length	f_1	Primary Mirror Focal Length (m)
M	Telescope Magnification	b_*	Telescope Back Focus (m)
p	Primary Mirror Intercept Point (m)	p'	Secondary to Cassegrain Focus (m)
B	Mirror Separation (m)	D_o	Primary Mirror Diameter (m)
D_p	Image Plane Size (m)	D_s	Secondary Mirror Diameter (m)
R_1	Radius of Curvature Primary Mirror (m)	R_2	Radius of Curvature Secondary Mirror (m)
z_1	Primary Mirror Surface Location (m)	z_2	Secondary Mirror Surface Location (m)
b_2	Paraboloid Parameter	k_{sb}	Surface Brightness Coefficient
L	Radiance of Asteroid (W/m^2/sr.)	h	Planck's Constant (m^{2}kg/s)
c	Speed of Light in Vacuum (m/s)	λ	Wavelength of Radiation (m)
k_B	Boltzmann Constant (m^{2}kg/s^2/K)	ϵ	Emissivity of Object
τ_{optics}	Optics Transmission Coefficient	r_{ast}	Asteroid Mean Radius (m)
τ_{int}	Exposure Time (s)	N	Number of Exposures
E	Irradiance (W/m^2)	λ_{max}	Peak Emission Wavelength (m)
ψ	Maximum Energy per Photon (J)	Φ	Photon Flux (photons/m^2/sec)
r_{ast}	Smallest Mean Radius of Asteroid (m)	T_{ast}	Temperature of the Asteroid (K)
R_{ast}	Distance from Sensor to Asteroid (m)	q	Charge of an Electron (coulombs)
b	Wien's Displacement Constant (m K)	G	Photoconductive gain of device

*Graduate Research Assistant, Asteroid Deflection Research Center, Department of Aerospace Engineering
†Vance Coffman Endowed Chair Professor, Asteroid Deflection Research Center, Department of Aerospace Engineering

η	Quantum Efficiency	I_{signal}	Signal Current (Amperes)
H_{signal}	Total Signal Elections	$n_{e,d}$	Dark Curr. for Detector (phot./pix./ s)
n_{pix}	Number of pixels	I_{dark}	Dark Current (A)
σ_{dark}	Total Dark Current Elections	σ_{shot}	Total Shot Noise Electrons
l_x, l_y	Length, Width of Detector (m)	l_z	Thickness of Detector (m)
ρ	Detector Resistivity (Ωm)	R_d	Resistance of Detector (Ω)
T_d	Temperature of the Detector (K)	$I_{johnson}$	Johnson Noise Current (A)
$\sigma_{johnson}$	Total Johnson Current Elections	A_d	Area of the Detector's Face (m^2)
I_{GR}	Gen.-Recombination (GR) Noise Cur. (A)	σ_{GR}	Total GR Current Elections
$\bar{n}$	Average Num. of Photons from Source	σ	Standard Deviation of Photon Stream
S/N	Signal-to-Noise Ratio	K	Arbitrary Constant

I. Introduction

The Asteroid Deflection Research Center (ADRC) at Iowa State University has been developing a Hypervelocity Asteroid Intercept Vehicle (HAIV) concept against the most probable impact threat of asteroids with short warning time [1, 2, 3]. An illustration of the proposed HAIV terminal intercept scenario is provided in Figure 1. To demonstrate the feasibility of such a mission, a scaled polyhedron model of 433 Eros was used in [4] for a closed-loop optical navigation and guidance simulation study of the HAIV concept. This, however, did not consider the possibility of implementing an infrared telescope if visual detection would not be sufficient. When visual tracking is not available, as seen in Figure 2, a telescope and infrared sensor might be required for a precision impact and mission success.

An infrared sensor array has been employed on the Exoatmospheric Kill Vehicle (EKV). This vehicle is used to intercept ballistic missiles at high speeds. The on-board focal plane array used for targeting consists of a 256 by 256 structure with pixel pitch of 30 μm that are sensitive to long wave (7 to 12 μm) or very long wave (12 to 30 μm) infrared emission [5]. During the vehicle's targeting process, it receives information from the Space Based Infrared Sensor (SBIRS) low earth

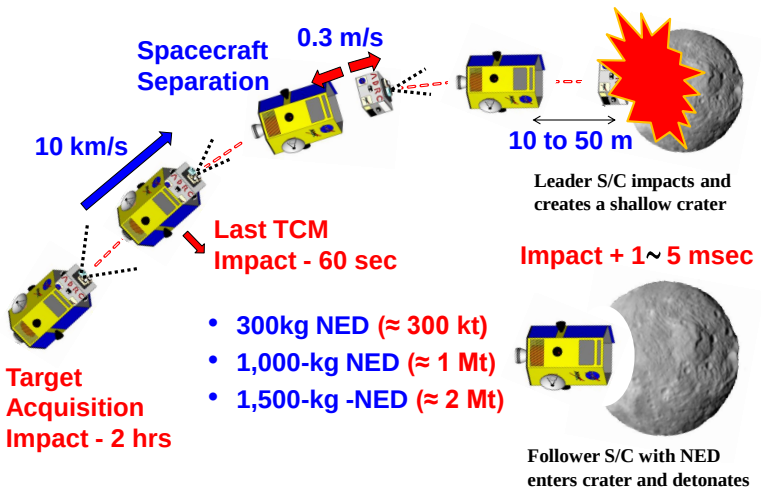

Figure 1. A baseline terminal intercept scenario of a two-body HAIV carrying a nuclear explosive device (NED) [1, 2, 3].

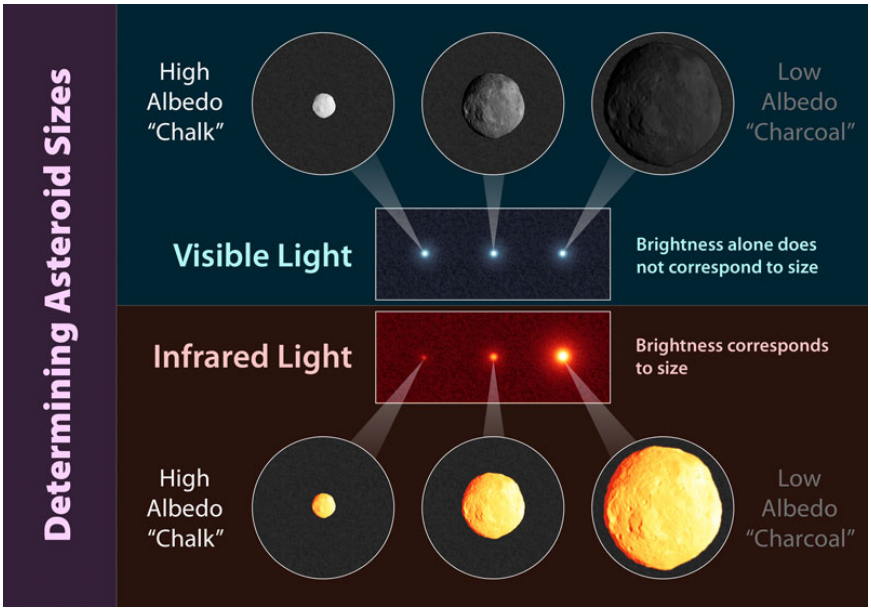

Figure 2. Comparisons of optical and infrared images of asteroids with different sizes and albedos. Image courtesy of `http://wise.ssl.berkeley.edu/gallery_asteroid_sizes.html`

orbit long wave infrared sensor. By using this sensor, and unknown optics, the detection range of the system is said to be about $1000e6$ kilometers for an object emitting $6e8$ W/Ster. However, exact details on the signal-to-noise ratio value for object detection and mission success for both the EKV and SBIRS are unknown [6].

It has been shown in [7] what physical models are needed to estimate the signal-to-noise ratio for a given detector and asteroid scenario in the N-band of infrared wavelength. This procedure did not entirely take into account the optics of the instrument and uses a different definition for the signal-to-noise ratio. To remedy the optics situation, there can be different telescope designs

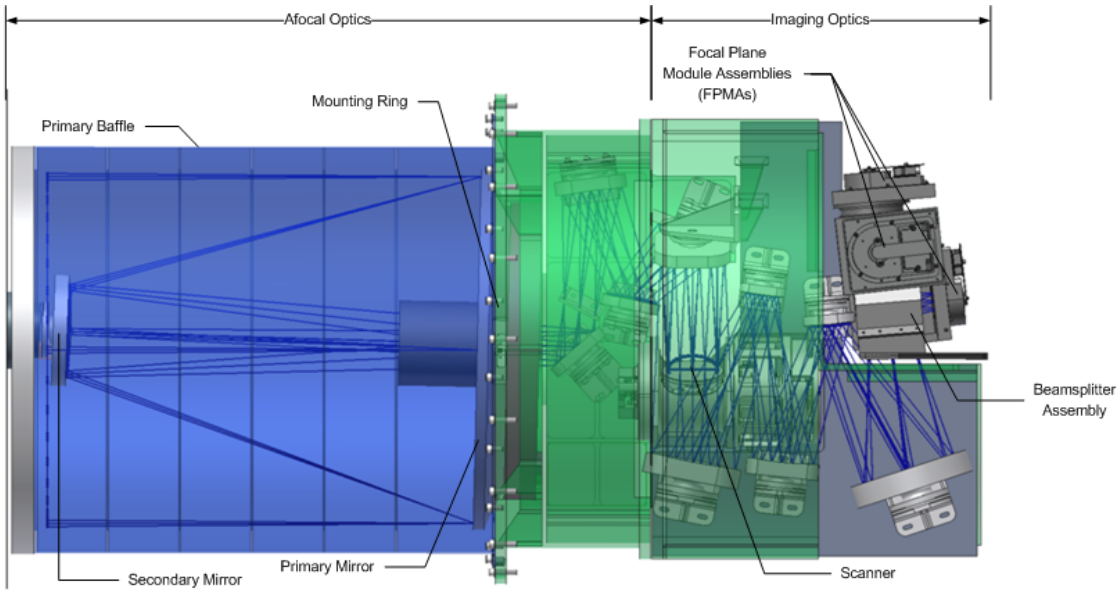

Figure 3. Illustration of WISE telescope [8].

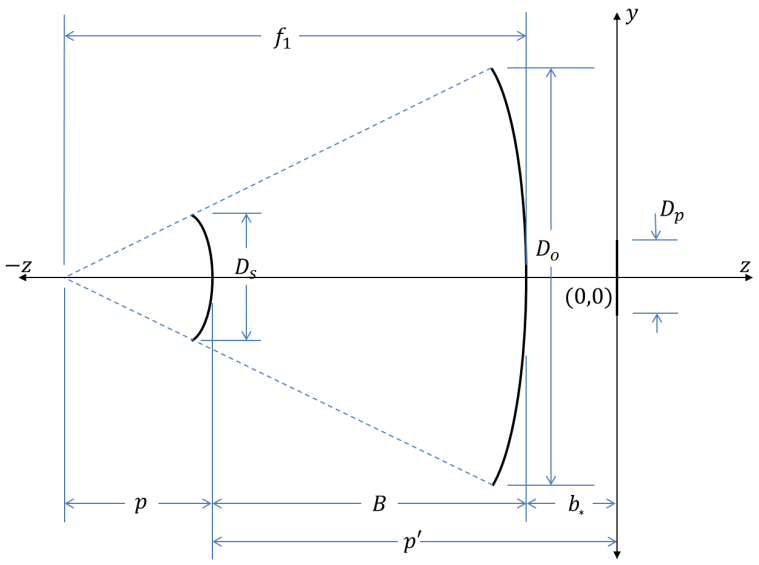

Figure 4. Classical Cassegrain telescope design.

explored. A reference infrared telescope, the Wide-field Infrared Survey Explorer (WISE), uses a Cassegrain like primary mirror to collect signal from objects of interest. An image that references the WISE telescope can be seen in Figure 3 [8].

II. Classical Cassegrain Telescope Design

While other instruments are needed, one solution for the navigation cameras is to implement a compact telescope design to meet the specifications of the terminal guidance. Here, a classical Cassegrain telescope design is considered. This system is investigated due to its simplicity and similarity to the (NEO)WISE infrared telescope design. An illustration of the Cassegrain telescope is given in Figure 4, which will be the basis of the instrument's parameters. To determine the characteristics for this implement, the variables given by this diagram are solved, given an effective focal length, primary mirror focal length and diameter, and back focus distance. It can be seen that baffling and glare stops were not taken into account. At this time, these design specifics are not being factored in.

The magnification of the system is found first. This is simply done by dividing the focal length of the system, F, by the primary mirror's focal length, f_1, which gives

$$M = \frac{F}{f_1} \tag{1}$$

Once magnification is calculated, other parameters of this system are found. Given the back focus (distance from the primary mirror to the focal plane), b_*, the primary mirror focus intercept point is found as

$$p = \frac{F + b_*}{M + 1} \tag{2}$$

The overall distance from the secondary mirror to the focal plane, also known as the secondary

to Cassegrain focus p', follows directly from the primary focus. Since the magnification is the first value found, p' is simply

$$p' = pM \tag{3}$$

From the Cassegrain focus, the mirror separation, B, is found as

$$B = p' - b_* \tag{4}$$

Another very important part of the Cassegrain telescope is to design the size of the secondary mirror. This diameter, D_s, can be found as

$$D_s = \frac{pD_o}{f_1} + \frac{BD_p}{f_1 M} \tag{5}$$

where D_p is the image plane size. This correlates to the size of the imaging device, which is equivalent to the minimum dimension of the array. An example will be given in the NEOWISE Instrument section. Equations (2) to (5) are given in Beish [9].

With these parameter distances known, the radius of curvature (ROC) is found for both the primary and secondary mirrors. The primary mirror, since it is a paraboloid, is given by

$$R_1 = 2f_1 \tag{6}$$

and

$$R_2 = \frac{2}{\frac{1}{p} - \frac{1}{p'}} \tag{7}$$

where R_1 is the ROC for the primary mirror and R_2 is the ROC for the secondary mirror [10, 11]. By using the ROC's of each mirror, the prescription for the two mirrors can be found by the formulas

$$z_1 = \frac{y_1^2}{2R_1} - b_* \tag{8}$$

$$z_2 = \frac{y_2^2/R_2}{1 + \sqrt{1 - (1 + b_2)(y_2/R_2)^2}} - (b_* + B) \tag{9}$$

and

$$b_2 = \frac{-4M}{(M-1)^2} - 1 \tag{10}$$

where z_1 and z_2 are face locations of the mirrors when the image plane array is at the origin of a measurement, $\frac{-D_o}{2} \leq y_1 \leq \frac{-D_0}{2}$, and $\frac{-D_s}{2} \leq y_2 \leq \frac{-D_s}{2}$ [11]. This is only valid for the case of a Classical Cassegrain telescope. With all of the basic parameters known, an important coefficient is then calculated.

When looking through a telescope, the magnification, primary mirror diameter, and image plane size (array size or eye pupil diameter) make a difference on the brightness of the image. The brightness coefficient takes into account the light grasp and magnification of the device to give the maximum amount of light that is illuminating the device. This is given in [12] by

$$k_{sb} = \left(\frac{D_o}{MD_p}\right)^2 \tag{11}$$

A way to interpret this coefficient is to use the same telescope but different eye pieces to enlarge the image size at the entrance of the eye pupil. This spreads the same amount of light out onto a larger area, hence creating a dimmer object.

III. Signal-to-Noise Ratio

The IR detector array receives signals from the asteroid, and the sensor array wells are filled. While the signal is obtained from the asteroid, the detector also has noise and dark current values, which is said to be total detector noise. Since the frequencies of this noise are unknown, the approximation for the signal-to-noise ratio (SNR) is computed. Once the value of the SNR reaches a mission selected value, the object in question, here an asteroid, is said to be able to be detected. To simulate these values, approximation of blackbody radiation signal current and noise signal current are calculated.

A. Signal Analysis

A step in approximating the asteroid signal requires the integration of Planck's law over the detectable wavelength band of the IR detector. Black body radiation for different temperature values is shown in Figure 5. The form of Planck's law used here is a function of the wavelength. While there are multiple bands for the wavelengths, the focus here is on objects that are in the 250 Kelvin range [13]. For this case, the wavelengths being used start at the Mid Infrared N band (7.5-14.5 μm) and extend to 16.5 μm, which is used for the W3 band given for the WISE telescope in section 3, number 2, Table 1 [14]. This gives radiance of the asteroid with integration bounds as

$$L = \int_{\lambda_1}^{\lambda_2} \epsilon \frac{2hc}{\lambda^5} \frac{1}{e^{\frac{hc}{k_b T_{ast} \lambda}} - 1} d\lambda \tag{12}$$

where h is Planck's constant, k_b is Boltzmann constant, and c is the speed of light.

Once the radiance is found, the irradiance on the detector can be calculated. This takes into account the solid angle subtended by a circular approximation of the asteroid. The irradiance is then given by

$$E = \frac{L\pi r_{ast}^2}{d_{ast}^2} \tag{13}$$

To calculate the signal current, the irradiance needs to be converted into a photon flux. This will compute the minimum amount of electrons passing through the aperture. The Wien's displacement law for finding the wavelength of peak emission is given by

$$\lambda_{max} = b/T_{ast} \tag{14}$$

where λ_{max} is the maximum energy per photon, in Joules, and

$$\psi = \frac{hc}{\lambda_{max}} \tag{15}$$

The photon flux, which is the amount of photons passing through one square meter, can be determined by dividing the irradiance by the maximum energy per photon at the desired wavelength. This gives the photon flux as

$$\Phi = \frac{E}{\psi} \tag{16}$$

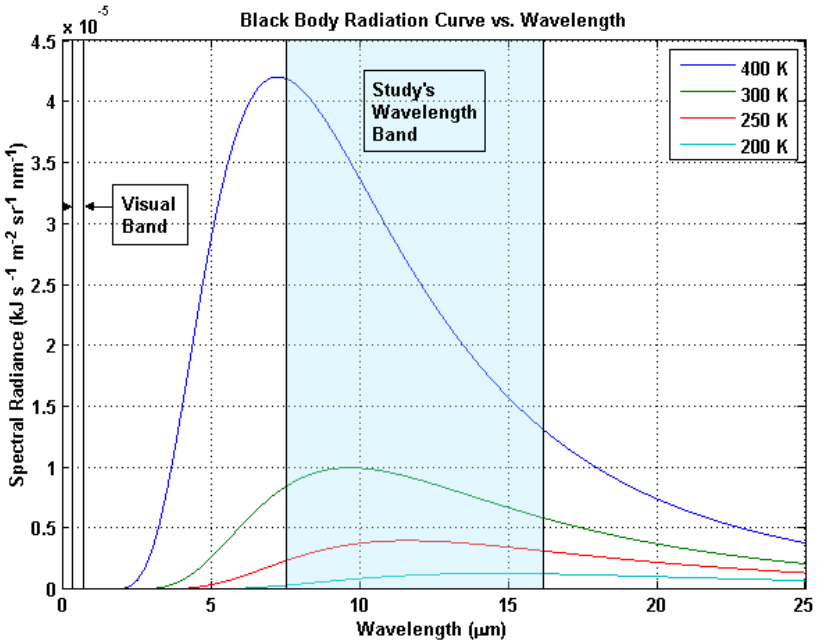

Figure 5. Black body radiation for different temperature values.

Then by using telescope and detector array parameters, the photon flux is manipulated into the signal current. This is given by this alternate equation from that given by Rieke [15] as

$$I_{signal} = k_{sb}\left(\frac{L\pi r_{ast}^2 b}{d_{ast}^2 hcT_{ast}}\pi\left(\frac{D_o}{2}\right)^2 \tau_{optics}\right) q\eta G \tag{17}$$

which takes into account the objects solid angle, max frequency emission given by Wien's displacement law, and the effects of the surface brightness due to the optics. The variable τ_{optics} is estimated to be at 0.504 in the optical by Schott [16]. This is assumed to be the transmission coefficient in the IR range as well. However, it would be advantageous to know the number of electrons being excited for a given amount of time and number of exposures. A new form of the above equation can be given by

$$H_{signal} = k_{sb}\left(\frac{L\pi r_{ast}^2 b}{d_{ast}^2 hcT_{ast}}\pi\left(\frac{D_o}{2}\right)^2 \tau_{optics}\right) \eta G N \tau_{int} \tag{18}$$

where N is the number of exposures and H_{signal} is given in number of electrons.

B. Noise Current

One of the most important aspects of signal processing is the amount of noise in the system. If there is too much noise and the noise signal is not known, it would be virtually impossible to differentiate from correct or incorrect data. The following analysis incorporates four places where there could be unwanted current added to the system. This, for generality, will be called a noisy current.

1. *Dark Current Noise*

Dark current noise is assumed to follow Poisson statistics, therefore the current is given by the standard deviation form

$$I_{dark} = \sqrt{n_{e,d} n_{pix} q} \tag{19}$$

but this does not take into account the number of exposures and exposure time. By looking at a Poisson process, the standard deviation is related to the duration of the total sampling. The dark current deviation, in number of electrons given by [17], can then be written in a slightly different form,

$$\sigma_{dark} = \sqrt{n_{e,d} n_{pix} N \tau_{int}} \tag{20}$$

where σ_{dark} is also given in number of electrons.

2. *Shot Noise*

Much like the Dark current noise, shot noise follows a Poisson process as well. This noise comes from the total number of detected photons, which emit from the target. The equation, incorporating the number of exposures and exposure time, is then in a slightly different form than given by Bolte [17], which leads to

$$\sigma_{shot} = \sqrt{H_{signal}} \tag{21}$$

where σ_{shot} is given in the total number of electrons.

3. *Johnson Noise*

Johnson noise is noise in the detector due to resistance of the material, described by [7] as

$$I_{johnson} = \sqrt{\frac{2 k_B T_d}{R_d \tau_{int}}} \tag{22}$$

and

$$R_d = \frac{\rho l_y}{l_x l_z} \tag{23}$$

A depiction of an array cell can be seen in Figure 6. Again, the current needs to be changed into number of electrons and also with respect to the number of exposures and exposure duration. This

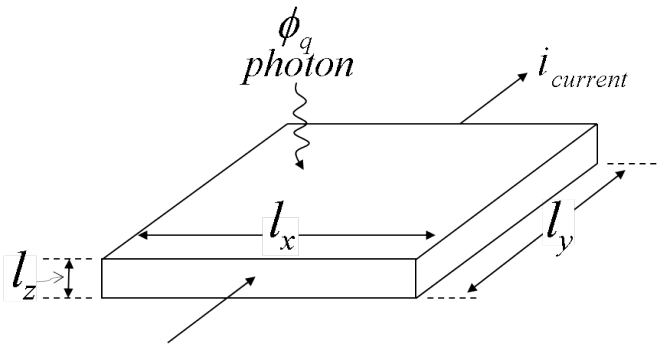

Figure 6. A simple diagram of sensor characteristics.

would represent the standard deviation in number of electrons, using Poisson statistics, which then yields

$$\sigma_{johnson} = \sqrt{\frac{2k_B T_d N \tau_{int}}{R_d q^2}} \tag{24}$$

4. *Generation-Recombination Noise*

Generation-Recombination noise is the result of generation and recombination of charged particles within the detector material. Dereniak and Boreman [18] give the following equation to calculate the current generated in the sensor array:

$$I_{GR} = 2qG\sqrt{\frac{\eta \Phi \tau_{optics} A_d}{2\tau_{int}}} \tag{25}$$

However, this is given in amperes and does not include the number of exposures. An alternate form is then found for Generation-Recombination deviation following Poisson process. This form, in number of electrons, given by

$$\sigma_{GR} = G\sqrt{2\eta \Phi \tau_{optics} A_d N \tau_{int}} \tag{26}$$

C. SNR Calculation

Dereniak and Boreman [18] give a signal-to-noise ratio formula, which is given here in a similar form by

$$S/N = \frac{\text{average number of photons from source}}{\text{standard deviation of the photon stream}} = \frac{\bar{n}}{\sigma} \tag{27}$$

The standard deviation can be written as the square root of the sum of the squares for each noise component. This can only be done due to each noise signal being uncorrelated. Also, by using H_{signal} as the average photons from the source, the signal-to-noise ratio can be written in the form of

$$S/N = \frac{H_{signal}}{\sqrt{\sigma_{dark}^2 + \sigma_{shot}^2 + \sigma_{johnson}^2 + \sigma_{GR}^2}} \tag{28}$$

With factoring out the exposure time and number of exposures, assuming no telescope variables, distances, or object parameters are changing, an alternate form for the above equation is given by

$$S/N = K\sqrt{N\tau_{int}} \tag{29}$$

where K is a constant. This shows that the signal-to-noise ratio increases with the square root of the product of exposure time and number of exposures.

IV. HAIV IR Telescope Design and NEOWISE Instrument

A. NEOWISE Instrument

Wright [19] states that the NEOWISE can detect a 250 meter diameter size object at approximately 0.5 AU. However, Wright did not mention the exposure time that would be used nor the signal-to-noise ratio desired. Yet, to confirm this detection, values given in [7, 8, 20, 21] are used to

calculate the signal-to-noise ratio developed in this paper. Table 1 shows sensor array and telescope parameters given from these sources. Since the total configuration of the NEOWISE telescope is not known, a classical Cassigrain telescope will be designed to calculate the signal-to-noise ratio. In Table 2, the signal-to-noise ratio is given.

Table 1. NEOWISE asteroid detection input data

Instrument Characteristics	Values	Asteroid Parameters	Value
F	1.35 m	T_{ast}	300 K
M	8	r_{ast}	125 m
D_o	0.4 m	d_{ast}	0.5 AU
η	0.7	ϵ	0.9
G	6.83		
τ_{optics}	0.504		
N	200		
τ_{int}	8.8 sec		
$n_{e,d}$	5 e/pix/sec		
n_{pix}	$1024 \times 1024 =$ 1048576 pixels		
R_d	$5.00e04\ \Omega$		
Pixel Pitch	18 μm		
$\lambda_1,\ \lambda_2$	7.5, 16.5 μm		

Table 2. NEOWISE asteroid detection results

Results	Value
Geometric Optics Pixel Fill	<1
SNR	6.623

As can be seen from the table, the signal-to-noise ratio is above the sensitivity value of 5 given in Mainzer [21]. A larger exposure time could be used, along with reduction in number of exposures, to obtain the same result. This leads to a belief of confirmation for the above formulations. Since these values check with that of the NEOWISE telescope, a preliminary design then can be performed for the HAIV mission scenario.

B. HAIV IR Telescope

The HAIV spacecraft is required to have sensory array data of the target, which is needed for the terminal guidance algorithm. This may require the object on the image plane to fill multiple pixels to ensure correct thrusting maneuvers for accurate targeting. Table 3 gives information on a selected telescope design using similar parameters from Table 1. Note that the mission scenario uses an object with a 50 meter diameter. As mentioned previously, in this mission, the spacecraft is traveling towards the asteroid at approximately 10 km/sec. Due to this velocity, long exposure times and number of exposures must be kept at a minimum. A simple solution is to operate the device at its maximum data collection rate and use only one exposure. A typical high-speed digital single-lens reflex (DSLR) camera can reach frame rates of 1000 Hertz. Since video is not being recorded, shutter speed is taken to be 1/1000 of a second.

Table 3. HAIV telescope parameters and mission data

Instrument Characteristics	Values	Asteroid Parameters	Value
F	8 m	T_{ast}	300 K
M	8	r_{ast}	25 m
D_o	0.4 m	d_{ast} at 2 hours	$7.2e4$ km
D_s	≈ 0.050 m	d_{ast} at 60 sec	600 km
B	≈ 0.88 m	ϵ	0.9
b	0.08 m		
N	1		
τ_{int}	0.001 sec		
$\lambda_1,\ \lambda_2$	7.5, 16.5 μm		

Table 4. Baseline design results

Results	Value
Geometric Optics Horz. Pixe Fill at 2 hours	≈ 1.5
SNR at 2 hours	$4.5e3$
Geometric Optics Horz. Pixel Fill at 60 sec	≈ 185
SNR at 60 sec	$9.8e5$

These values are generated with the assumption of perfect focusing for the telescope device. The pixel fill entry in Table 4 corresponds to the horizontal pixel illumination on the detector array. This assumes the largest dimension of the asteroid is on horizontal axis, but this does not need to be the case. For simplicity, this is done since the object can actually have any orientation on the image plane, which is that of the actual asteroid.

A computer generated image of the simulated telescope can be seen in Figure 7. This is a true scaled model where all dimensions are given in meters, and the origin of the axis is the location of the image plane. In this plot, the sun rays come from the negative optical axis, or with respect to the image, from the left.

This design than can be implemented into the mission scenario simulation. There it will be used in guidance of the spacecraft, for the terminal phase of the mission, to ensure impact of the asteroid.

V. Closed-Loop Guidance Simulations

To impact such a small object at hypervelocity speeds, it requires a precision guidance system. This section shows guidance and impact simulations done on an asteroid using a visual camera and an IR camera including the preliminary HAIV telescope described in the previous section.

As mentioned previously, the pixel fill values found were for an asteroid that is 50 meter diameter. A simulated IR and visual image, of this size asteroid, can be seen in Figure 8, which

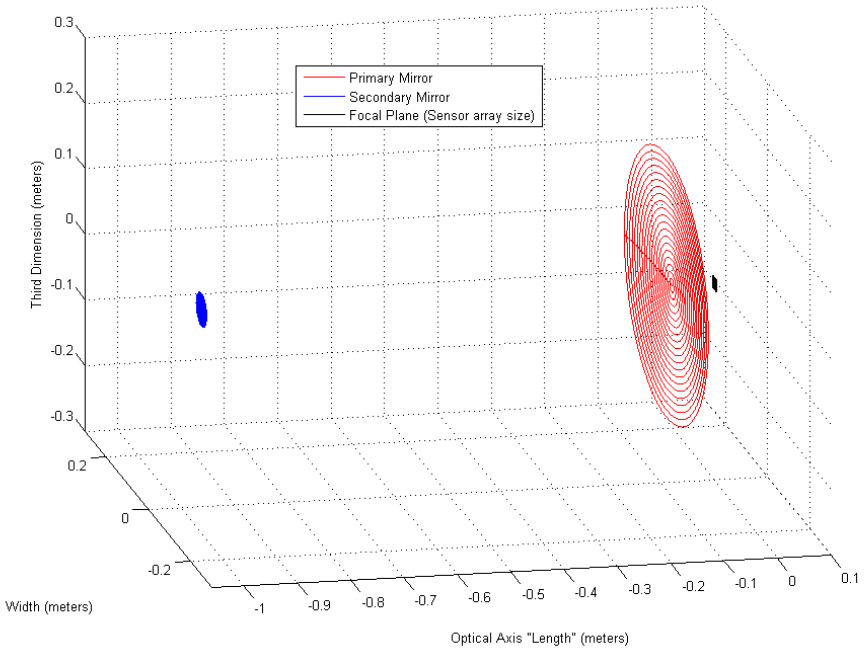

Figure 7. 3 D plot of the mirror surfaces and sensor array for the HAIV Cassegrain telescope.

correspondences to what is sensed at 60 seconds before impact for each camera (these images are cropped so that they can be seen better). It can be seen in this figure that there is a pink plus on each image. This mark is the targeted impact location of each sensor. These points are the Center of Figure (COF) of the IR image and Center of Brightness (COB) for the Visual image. The terminal guidance system uses this information to calculate the thrusting maneuvers.

For the HAIV scenario, a hybrid guidance scheme is used for maneuvers. There are 3 predeter-

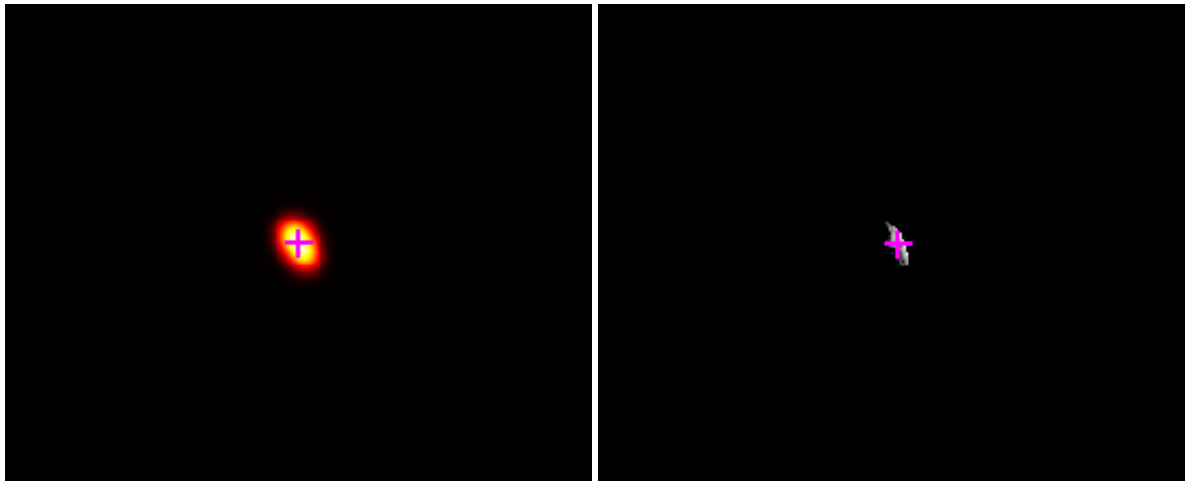

a) Simulated IR image **b) Simulated visual image**

Figure 8. Two examples of IR and visual camera at 60 seconds before asteroid intercept.

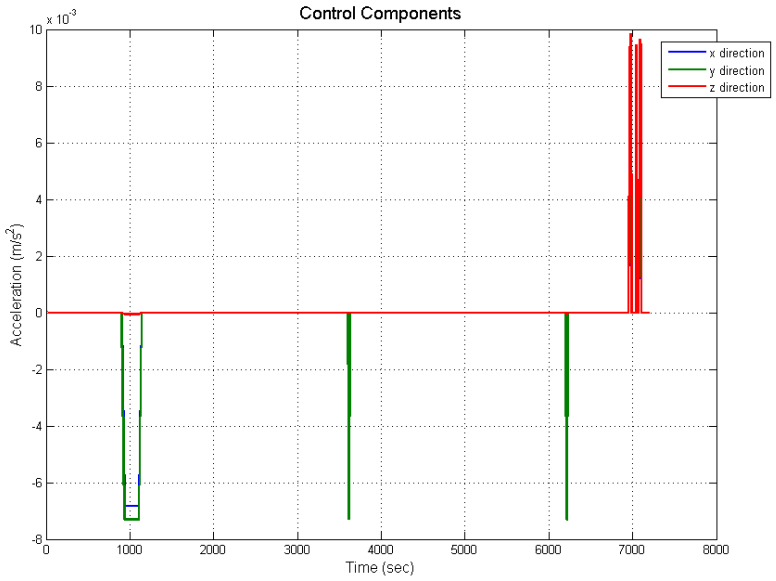

Figure 9. IR simulation thrusting maneuver components.

mined pulses scheduled at 6300, 3600, and 1000 seconds before impact, which are implemented using kinematic impulse (KI) guidance taken from Hawkins [22]. After this is completed, the system switches over to closed-loop PN guidance at the last 270 seconds before impact. In addition, there is no thrusting control when the time before impact is less than 60 seconds. This is due to the spacecraft separating into the fore and aft bodies. These thrusting components found from the hybrid scheme can be seen in Figures 9 and 10.

In these figures, the PN guidance scheme performs better in the IR image scenario than that of the visual image. This is primarily due to the target location of the IR image being very close

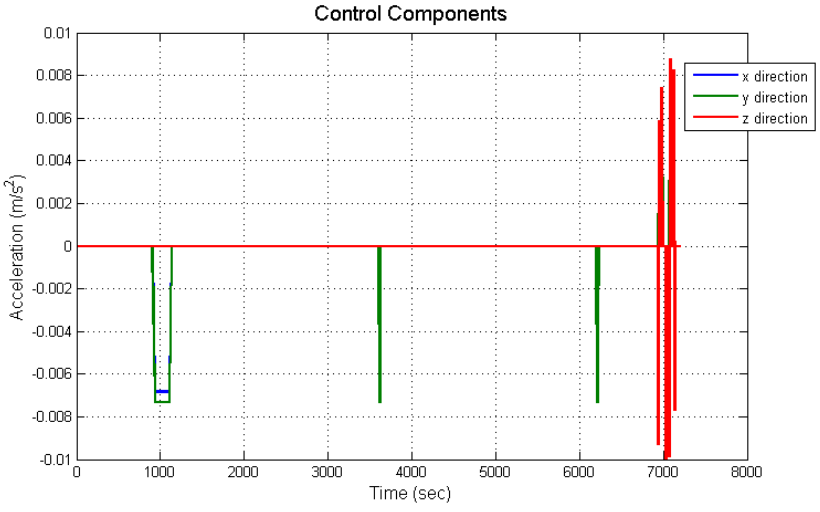

Figure 10. Visual simulation thrusting maneuver components.

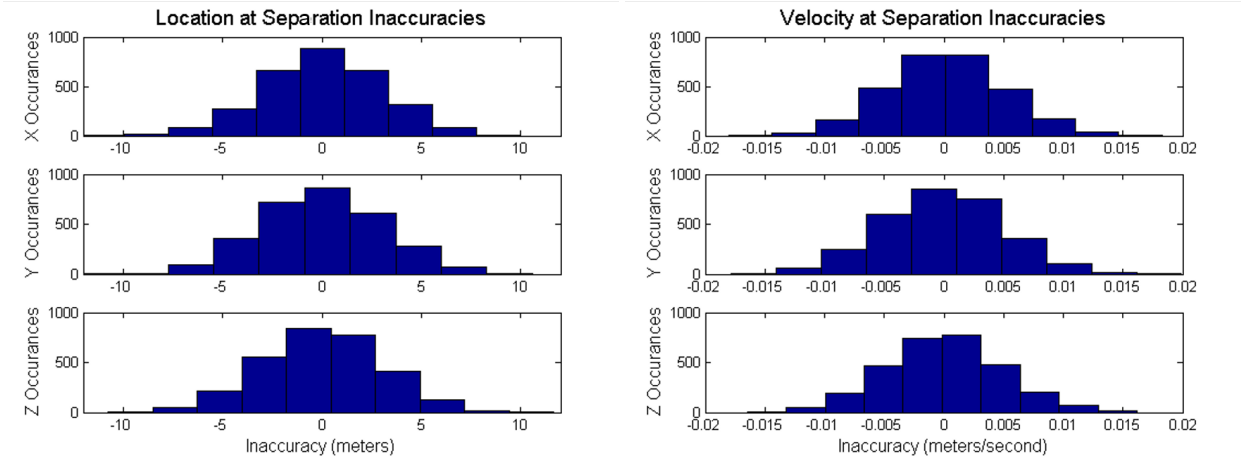

a) Position error **b) Velocity error**

Figure 11. IR scenario position and velocity errors at 60 seconds before asteroid intercept.

to that of the center of mass for the asteroid. Yet, in both cases the x and y thrusting components are corrected by the KI guidance, but the z direction has minimal velocity change. Overall, for the thrusting component scheme, it would be easier to implement the IR camera due to the difficulty in PN thrusting directions for the visual case. Both scenarios, visual and IR, undergo an impact simulation, regardless of the complexity of thrusting maneuvers.

A Monte Carlo impact simulation was conducted after the spacecraft separates at 60 seconds before impact. At separation time, a position and velocity error are included. Images of the error distributions are given in Figure 11. Similar normal distributed values are seen by the visual simulations as well. Using these error values for impact simulation, it was observed that in 3000

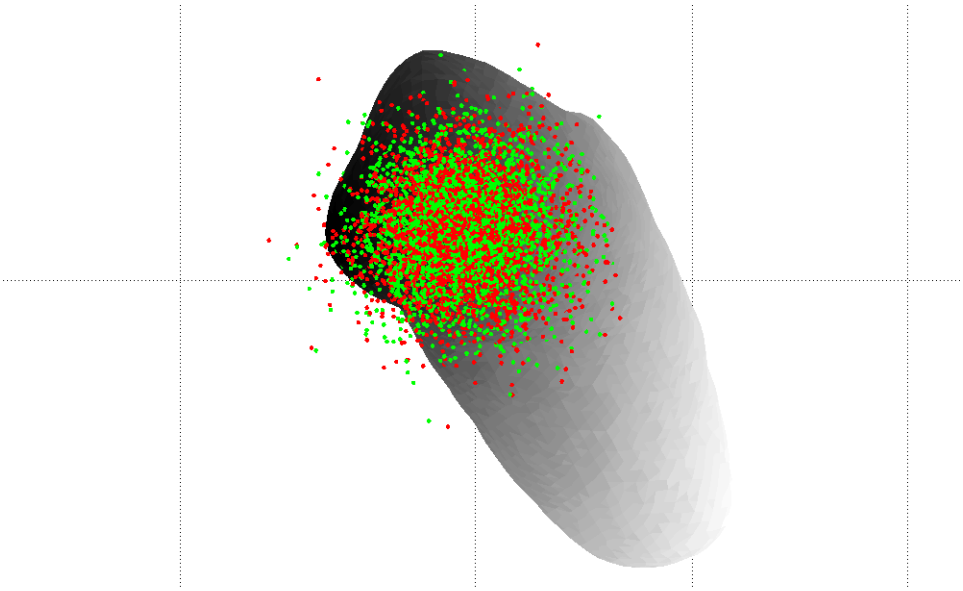

Figure 12. 50 m asteroid impact distribution.

runs, the IR camera guidance outperformed the visual camera. Approximately 98.5 percent of the fore bodies and 98.7 percent of the aft bodies impacted for the IR case. Whereas only 93.4 percent impacted of both fore and aft bodies for the visual case. An image of the impact distribution on the asteroid is given in Figure 12 where the fore body is green, and the aft body is red. For such a small asteroid, a single spacecraft kinetic impacter may suffice, but separation simulations are conducted for proof of concept.

VI. Future Work

Future work for this project is to incorporate Seidel aberrations, theoretical optical resolution limit, and also include other telescope types to try and improve telescope performance. With this, an inclusion of image post processing will help in the terminal guidance algorithm to potential increase mission success.

VII. Conclusion

This work has shown that the estimated signal-to-noise ratio and incorporation of an optical system is reliable when applied to the confirmation of detection distance for the NEOWISE telescope. By following the same equations for telescope design and signal-to-noise ratio formulation, a preliminary design for an optical system was created for the HAIV mission, which was suitable in a 50 m asteroid detection and imaging for the intercept scenario. Using the determined telescope and sensor parameters, it was shown that a hybrid 3 pulse and PN guidance scheme can be implemented to ensure high impact probability. Impact probability was obtained by simulations for both the IR and visual cases. It was found that the visual scenario had difficult thrusting maneuvers and underperformed the IR scheme. The IR case was able to impact the asteroid, when inaccuracies were incorporated at separation time, with approximately 98.5 percent.

References

[1] Wie, B. "Hypervelocity Nuclear Interceptors for Asteroid Disruption," Acta Astronautica, 90, 2013, pp. 146-155.

[2] Pitz, A., Kaplinger, B., Vardaxis, G., Winkler, T., and Wie, B., "Conceptual Design of a Hypervelocity Asteroid Intercept Vehicle (HAIV) and Its Flight Validation Mission," Acta Astronautica, 94, 2014, pp. 42-56.

[3] Barbee, B., Wie, B., Steiner, M., and Getzandanner, K., "Conceptual Design of HAIV Flight Demonstration Mission," AIAA-2013-4544, AIAA Guidance, Navigation, and Control Conference, Boston, MA, August 19-22, 2013.

[4] Lyzhoft, J., Hawkins, M., Kaplinger, B., and Wie, B., "GPU-Based Optical Navigation and Terminal Guidance Simulation of a Hypervelocity Asteroid Impact Vehicle (HAIV)," AIAA-2013-4966, AIAA Guidance, Navigation, and Control Conference, Boston, MA, August 19-22, 2013.

[5] Herring, J., and et al. *Staring 256 X 256 LWIR Focal Plane Array Performance of the Raytheon Exoatmospheric Kill Vehicle*. Conference Proceedings. N.p.: n.p., 1998. Print.

[6] Sessler, A. M., et al. *Countermeasures: A Technical Evaluation of the Operational Effectiveness of the Planned US National Missile Defense System*. Cambridge: Union of Concerned Scientists MIT Security Studies Program, Apr. 2000. PDF

[7] Lyzhoft, J., Groath, D., and Wie, B., "Optical and Infrared Sensor Fusion for Hypervelocity Asteroid Intercept Guidance," AAS 14-421, AAS/AIAA Space Flight Mechanics Meeting, Santa Fe, NM, January 26-30, 2014.

[8] "WISE Preliminary Release Explanatory Supplement: WISE Flight System and Operations." *WISE Preliminary Release Explanatory Supplement*. N.p., 12 Apr. 2011. Web. 7 Apr. 2014. http://wise2.ipac.caltech.edu/docs/release/prelim/expsup/sec3_2.html.

[9] Beish, J. D., *Cassegrain Telescopes for Amateurs*. 3 Dec. 2013. PDF.

[10] Shaw, J. A., "Reflector Telescopes." Class Lecture, Optical System Design, Montana State University, Bozeman, Febuary 4,2009.

[11] Lockwood, M. E., "Cassegrain Formulas and Tips by Mike Lockwood." *Lockwood Custom Optics*. N.p., n.d. Web. 5 May 2014. http://www.loptics.com/ATM/mirror_making/cass_info/cass_info.html.

[12] Culp, R., *Telescope Image Brightness*. N.p.: n.p., 2 May 2014. DOC.

[13] National Aeronautics and Space Administration, "Near Earth Asteroid Rendezvous (NEAR) Press Kit," http://www.nasa.gov/home/hqnews/presskit/1996/NEAR_Press_Kit/NEARpk.txt [cited 14 September 2013].

[14] Cutri, R. M. et al., "Explanatory Supplement to the WISE Preliminary Data Release Products," http://wise2.ipac.caltech.edu/docs/release/prelim/expsup/wise_prelrel_toc.html [cited 29 July 2013].

[15] Rieke, J. H., *Detection of Light: from the Ultraviolet to the Sub-millimeter*, 1st ed., Cambridge University Press, New York, 1994, pp. 56.

[16] Schott, J. R., *Remote Sensing: The Image Chain Approach*, 1st ed., Oxford University Press, New York, 1997, pp. 184.

[17] Bolte, Michael Dr., "Signal-to-Noise in Optical Astronomy." Class Lecture, Modern Observational Techniques, University of California, Santa Cruz, n.d.

[18] Dereniak, E. L., Boreman, G. D., *Infrared Detectors and Systems*, John Wiley & Sons, New York, 1996, Ch. 5.

[19] Wright, E. L., et al., "The Wide-Field Infrared Survey Explorer (WISE): Mission Description and Initial On-Orbit Performance," *The Astronomical Journal*, Vol. 140, No. 6, 2010, pp. 1868.

[20] "WISE Preliminary Release Explanatory Supplement: Introduction." *WISE Preliminary Release Explanatory Supplement*. N.p., 17 Aug. 2011. Web. 13 Apr. 2014. http://wise2.ipac.caltech.edu/docs/release/allsky/expsup/sec1_1.html#wise.

[21] Mainzer, A. K. et al., *Preliminary Design of The Wide-Field Infrared Survey Explorer (WISE)*. San Diego: SPIE, 10 Aug. 2005. PDF.

[22] Hawkins, M., Guo, Y., and Wie, B., Spacecraft Guidance Algorithms for Asteroid Intercept and Rendezvous Missions, International Journal of Aeronautical and Space Sciences, Vol. 13, No. 2, June 2012, pp. 154-169.